

POD-based background removal for particle image velocimetry

M.A. Mendez ^{a,*}, M. Raiola ^b, A. Masullo ^c, S. Discetti ^b, A. Ianiro ^b, R. Theunissen ^c, J.-M. Buchlin ^a

^a von Karman Institute for Fluid Dynamics, Waterloosesteenweg 72, Sint-Genesius-Rode, Belgium

^b Aerospace Engineering Group, Universidad Carlos III de Madrid, Av. de la Universidad 30, Leganés, Spain

^c Department of Aerospace Engineering, University of Bristol, University Walk, BS81TR Bristol, UK



ARTICLE INFO

Article history:

Received 21 June 2016

Received in revised form 15 August 2016

Accepted 18 August 2016

Available online 20 August 2016

Keywords:

PIV image pre-processing

POD decomposition of video sequences

Reduced Order Modeling (ROM)

ABSTRACT

State-of-art preprocessing methods for Particle Image Velocimetry (PIV) are severely challenged by time-dependent light reflections and strongly non-uniform background. In this work, a novel image preprocessing method is proposed. The method is based on the Proper Orthogonal Decomposition (POD) of the image recording sequence and exploits the different spatial and temporal coherence of background and particles. After describing the theoretical framework, the method is tested on synthetic and experimental images, and compared with well-known pre-processing techniques in terms of image quality enhancement, improvements in the PIV interrogation and computational cost. The results show that, unlike existing techniques, the proposed method is robust in the presence of significant background noise intensity, gradients, and temporal oscillations. Moreover, the computational cost is one to two orders of magnitude lower than conventional image normalization methods. A downloadable version of the preprocessing toolbox has been made available at <http://seis.bris.ac.uk/~aexrt/PIVPODPreprocessing/>.

© 2016 Elsevier Inc. All rights reserved.

1. Introduction

Particle Image Velocimetry (PIV) has become a standard optical technique for flow velocity measurement. By recording the scattered laser light of small tracer particles dispersed in the flow, the velocity field is inferred by evaluating the displacement of particle images throughout the image recording. This is typically achieved by cross-correlating image portions in consecutive recordings [1–3]. Consequently, regardless of the statistical operator applied, the accuracy of PIV relies on the quality of the image, which constitute the measurement input signal. Under ideal conditions, PIV images consist of bright particles with a diameter of 2–3 pixels superimposed onto a dark background [4,5]. The correlation peak can thus be retrieved with a sub-pixel accuracy of the order of 0.01 pixels [6]. In real conditions, however, this accuracy is considerably lowered by a number of background noise sources which pollute the correlation map. Examples are uneven gray level offsets produced by laser light reflections originating from variations in refractive index within the experimental setup, or random noise produced by camera dark noise and light scattering between particles. The background noise reduces the particle contrast and yields spurious correlation peaks which may even exceed the sought-for particle displacement peak.

When PIV experiments are performed over opaque objects, proper material selection or adequate surface treatment can limit the prominence of reflections by reducing omnidirectional light scattering [7]. Alternatively, light reflections can be minimized by suitable camera observation angle [8]. These solutions are however not generally feasible and image quality is thus typically enhanced in the post-recording stage. Two common approaches are image *levelization* and *normalization*.

Levelization consists in subtracting from each PIV image a reference intensity map, representative of the background noise. Background images can be constructed from low-pass filtered versions of the images [9] or by considering each PIV frame as the reference intensity of the following [10,11]. Alternatively, when a sufficient number of recordings are available, reference images can be formulated on a statistical basis by considering the ensemble minimum intensity [12], the ensemble average [13] or the intensity probability density distribution [14]. *Normalization* consists in remapping the original intensity using the entire dynamic range available in order to maximize the contrast between particles and background. This re-mapping is accomplished via linear or non-linear transformations [15] and can be global, i.e. acting on the full image, or local, i.e. acting independently on small portions of the image [16–18]. An alternative to the full remapping is the intensity capping method proposed in [19], which limits the relative intensity of bright objects compared to particle intensities by setting an upper limit for the gray scale values of the images. Levelization and normalization approaches

* Corresponding author.

E-mail address: mendez@vki.ac.be (M.A. Mendez).

can also be combined, as in the min/max filtering technique proposed in [20,21]. In this method, the gray scales are normalized with respect to envelopes for the minimum and maximum intensities, determined within a $m \times n$ pixels neighborhood.

Despite the variety of existing pre-processing approaches, none of the mentioned methods perform satisfactorily when reflections are either too bright to be removed via normalization methods, largely time-varying, or too sharp to be removed by levelization methods. In these situations, one is obliged to combine the existing techniques, on a case-by-case basis, in complex image analysis schemes (e.g. [22,23]) or utilize temporal high pass filtering if the background noise source is temporally resolved, as is the case in most high-speed PIV experiments [24]. The final outcome is, in general, strongly dependent on the experience of the user [25].

In this paper, we propose a novel, robust and automatic preprocessing method to improve image quality independent of the image sequence temporal resolution, background noise sharpness or brightness. The proposed method for PIV image enhancement relies on the Proper Orthogonal Decomposition (POD) of the image sequence to construct a Reduced Order Model (ROM) which only retains the PIV particle pattern. The first reduced order modeling of a video sequence was proposed in [26], using Principal Component Analysis (PCA) to detect moving objects in the automatic video analysis. Since then, a large variety of ROM methods has been proposed in literature pertaining pattern recognition and video processing [27]. These methods consider the original video sequence, reshaped into a single matrix, as the sum of two components: a low-rank part, representative of static and large objects, and a sparse one, representative of small and moving objects. Such a decomposition is also the fundamental framework of matrix perturbation theory, with applications in finance [28], privacy preservation [29], pattern recognition [30] and more recently in the removal of random PIV velocity noise [31] or adaptive masking for PIV applications [32].

The POD framework for video sequences is recalled in Section 2, where several aspects of its application to PIV image pre-processing are described. These include the decomposition of an ideal PIV sequence (Section 2.1) and the removal of correlated background noise (Section 2.2). The proposed algorithm is presented in Section 2.3. Section 3 describes its application on synthetic and experimental test cases, and compares its performances to existing methods. The conclusions are reported in Section 4. A list of symbols is included in Appendix A.

2. POD decomposition of PIV image recordings

Let a PIV image sequence be composed of n_t grayscale images $Im(i,j) \in \mathbb{R}^{n_x \times n_y}$ having a resolution of $n_p = n_x n_y$ pixels. By reshaping each image into a column vector $s_i \in \mathbb{R}^{n_p \times 1}$, it is possible to assemble the sequence into a snapshots matrix X :

$$X = \{s_1, s_2, \dots, s_{n_t}\} \in \mathbb{R}^{n_p \times n_t}, \quad (1)$$

with n_p spatial realizations in the column space \mathbb{R}^{n_p} , and n_t temporal realization in the row space \mathbb{R}^{n_t} . The scope of low dimensional modeling (or low rank approximation) of matrix X is to find the approximation $\tilde{X} \in \mathbb{R}^{n_p \times n_t}$ of rank $r < \min(n_p, n_t)$ minimizing the L_2 norm ($\|\cdot\|$) of the error matrix E_r :

$$\min(E_r) = \min(\|X - \tilde{X}\|_2). \quad (2)$$

The solution to this minimization problem, given by the Eckart-Young theorem [33], is the r truncated singular value decomposition of the original matrix:

$$\tilde{X} = \Phi_r \Sigma_r \Psi_r^T \rightarrow \tilde{s}_i = \sum_{k=1}^r \phi_k \sigma_k \psi_k^i, \quad (3)$$

with $\Phi_r = [\phi_1, \dots, \phi_r] \in \mathbb{R}^{n_p \times r}$ the orthonormal basis for the columns of X , $\Psi_r = [\psi_1, \dots, \psi_r] \in \mathbb{R}^{n_t \times r}$ the orthonormal basis for the rows of X , and $\Sigma_r = diag(\sigma_1, \dots, \sigma_r) \in \mathbb{R}^{r \times r}$ the diagonal matrix containing the norm of each contribution. The orthonormality of these bases ensures that the error in Eq. (2) is minimal and that the decomposition is exact ($E_r = 0$) for $r = n_t$.

Eq. (3) is the discrete version of the Proper Orthogonal Decomposition (POD), also known as Karhunen-Loève decomposition [34], and can be interpreted as the decomposition of the original images s_i into the sum of $r < n_t$ spatial modes ϕ_k evolving with their corresponding temporal modes ψ_k . Each of these modal contributions $\phi_k \psi_k^T$ is a rank one ‘component’ of the original matrix, having optimal and sorted norm (energy) $\sigma_k > \sigma_{k+1} \forall k \in [1, n_t - 1]$.

In low rank modeling for video analysis, the images forming the spatial basis ϕ are referred to as *eigenbackgrounds* [26]. By definition, the ϕ_k are eigenvectors of the outer product matrix $C = XX^T \in \mathbb{R}^{n_p \times n_p}$ and the ψ_k are eigenvectors of the inner product matrix $K = X^T X \in \mathbb{R}^{n_t \times n_t}$, while the singular values σ_k are the square root of the corresponding eigenvalues λ_k :

$$C = XX^T = (\Phi \Sigma \Psi^T)(\Psi \Sigma \Phi^T) = \Phi \Lambda \Phi^T \quad (4a)$$

$$K = X^T X = (\Psi \Sigma \Phi^T)(\Phi \Sigma \Psi^T) = \Psi \Lambda \Psi^T \quad (4b)$$

The solutions to the eigenvalue problems expressed in Eqs. (4a) and (4b) are the discrete versions of the Fredholm equations, leading, respectively, to the definitions of standard POD [35] (preferable when $n_p \ll n_t$) or the Snapshot POD [36] (preferable when $n_t \ll n_p$). It should be noted that both definitions are common in the analysis of turbulent flows where instead of intensities, element entries of column vectors s_i refer to velocities.

Observing that $X \Psi_r = \Phi_r \Sigma_r$, Eq. (3) can be also written as:

$$\tilde{X} = \Phi_r \Phi_r^T X \rightarrow \tilde{s}_i = \sum_{k=1}^r (\phi_k^T s_i) \phi_k. \quad (5)$$

This form of the equation, with no emphasis on the temporal evolution of the modes, describes the decomposition as the projection of the data set (of rank n_t) into a lower dimensional space (of rank $r < n_t$) spanned by the orthonormal basis images $\Phi_r = [\phi_1, \dots, \phi_r]$. This formulation is common in Principal Component Analysis [37–39] where it is introduced in the framework of variance maximization or minimal error of the approximation matrix \tilde{X} [40–42].

The POD image preprocessing proposed in this work considers a PIV sequence as the sum of an ideal sequence X_p (i.e. bright particle images superimposed onto a black background) and a background noise sequence X_b , each having their own singular value decomposition:

$$X = \Phi \Sigma \Psi^T = X_p + X_b = \Phi_p \Sigma_p \Psi_p^T + \Phi_b \Sigma_b \Psi_b^T, \quad (6)$$

with $\Phi_p = [\phi_{p1}, \dots, \phi_{pn_t}]$ and $\Phi_b = [\phi_{b1}, \dots, \phi_{bn_t}]$ the eigenbackgrounds of X_p and X_b . Typical background noise in PIV has a high degree of spatial and temporal correlation, resulting in multiple rows and columns of X_b being similar to each others. Therefore, the matrix X_b is close to be rank deficient and can be well captured by few ($r \ll n_t$) of its modes, such that

$$X_b \approx \tilde{X}_b = \sum_{k=1}^r \phi_{bk} \sigma_{bk} \psi_{bk}^T | \sigma_{bk} \approx 0 \quad \forall k > r \ll n_t, \quad (7)$$

with $rank(\tilde{X}_b) = r \ll n_t$. It is worth observing that, besides allowing for the background noise to be time dependent – contrary to simple levelization approaches such as in [12,13] – the proposed method also allows for the video sequence to be temporally unresolved – contrary to time filtering approaches such as in [24].

A temporally unresolved sequence can in fact be constructed from column permutation of a time-resolved sequence, and the SVD decomposition in Eq. (3) – thus the approximation in Eq. (7) – is invariant under column permutation of the decomposed matrix.

From Eqs. (6) and (7), the proposed method consist in constructing an approximation of X_p and X_b using the POD modes of X . The method is based upon two assumptions, which are justified in Section 2.1 and Section 2.2, and validated in Sections 3.1 and 3.2:

Assumption 1. For $k > r$, the contribution of the ideal PIV sequence X_p is equally distributed, such that $\sigma_{pk} \approx \sigma_{pk+1} \forall k \in [r, n_t - 1]$.

Assumption 2. For $k > r$, the decomposition of the video X is aligned with that of the ideal PIV sequence X_p , such that $\sigma_k \approx \sigma_{pk} \forall k \in [r, n_t]$.

2.1. Decomposition of ideal PIV sequence

An ideal PIV image sequence, defined as $X_p = [s_{p1}, s_{p2}, \dots, s_{pn_p}]$, results in a matrix with negligible correlation between its columns, since particles are distributed randomly within an image. This implies that the temporal correlation matrix ρ_p is close to the identity matrix $I \in \mathbb{R}^{n_t \times n_t}$:

$$\rho_p^{ij} = \frac{\sum_{k=1}^{n_p} s_{pi}^k s_{pj}^k - n_p \mu_{s_{pi}} \mu_{s_{pj}}}{n_p \sigma_{s_{pi}} \sigma_{s_{pj}}} \approx I \quad (8)$$

where $\mu_{s_{pi}}$ and $\sigma_{s_{pi}}$ are the spatial averages and standard deviation in each ideal image s_{pi} . Considering these images as large realizations (samples) of a random variable, statistical convergence is reached such that $\mu_{s_{pi}} \approx \mu_{sp}$ and $\sigma_{s_{pi}} \approx \sigma_{sp} \forall i \in [0, n_t]$. Using the inner product notation $\sum_{k=1}^{n_p} s_{pi}^k s_{pj}^k = s_{pi}^T s_{pj}$, the inner product matrix $K_p \in \mathbb{R}^{n_t \times n_t}$ of the ideal PIV sequence is readily obtained from Eq. (8):

$$K_p = X_p^T X_p \approx n_p (\mu_{sp}^2 \underline{1} + \sigma_{sp}^2 I) \quad (9)$$

where $\underline{1} \in \mathbb{R}^{n_t \times n_t}$ is a square matrix of ones and $I \in \mathbb{R}^{n_t \times n_t}$ is the identity matrix of equal size.

The diagonalization of K_p , in line with Eq. (4b), gives the temporal basis Ψ_p of the ideal PIV sequence and the corresponding amplitudes $\Sigma_p = \sqrt{\Lambda_p}$. This matrix has only two eigenvalues with multiplicities $m(\lambda_{p1}) = 1$ and $m(\lambda_{p2}) = n_t - 1$ respectively. The corresponding singular values $\sigma_{pk} = \sqrt{\lambda_{pk}}$ are:

$$\sigma_{p1} = \sqrt{(\mu_{sp}^2 n_t + \sigma_{sp}^2) n_p} \quad (10a)$$

$$\sigma_{pk} = \sqrt{n_p} \sigma_{sp} \quad \forall k > 1 \quad (10b)$$

Eq. (10b) thus proves Assumption 1. Moreover, it is worth noting that the first POD mode has a constant temporal evolution since $K_p \psi_{p1} = \lambda_{p1} \psi_{p1}$ holds for $\psi_{p1} = \underline{1} \in \mathbb{R}^{n_t \times 1}$. Therefore, observing from Eq. (3) that $\phi_{p1} = X_p \psi_{p1} / \sqrt{\sigma_{p1}}$, it is easy to show that the first eigenbackground of the ideal PIV sequence is proportional to the temporal average of the particle pattern. Eq. (10b) gives a first necessary condition for a set of POD modes to be representative of an ideal PIV particle pattern: with the only exception of the first mode, all the singular values should be equal. This condition, on the other hand, makes the choice of the eigenvectors $\psi_k, \forall k > 1$ not unique. However, K_p being symmetric and positive definite, a full set of n_t orthonormal eigenvectors exists, such that $\psi_{pi}^T \psi_{pj} = \delta^{ij}$, with δ^{ij} the Kronecker delta. Therefore, the orthonor-

mality of any temporal eigenvector ψ_{pk} to the constant vector $\psi_{p1} = \underline{1}$ gives a second necessary condition for a POD mode to be linked to the particle pattern: since $\langle \psi_k, \underline{1} \rangle = \sum_{j=1}^{n_t} \psi_k^j = 0$, the corresponding temporal evolution should have zero mean. These two constraints allow for verifying whether a subset of POD modes of the image sequence can be used to approximate PIV particle patterns.

2.2. Removal of correlated background noise

The dependence of the singular values of the sequence (σ) on those of the background (σ_b) and the particle pattern (σ_p , cf. Eq. (10)) in Eq. (6) can be analyzed in the diagonalized form of the video sequence inner product matrix K :

$$K = X^T X = \underbrace{X_p^T X_p}_{K_p} + \underbrace{X_b^T X_b}_{K_b} + \underbrace{X_b^T X_p}_{K_{bp}} + \underbrace{X_p^T X_b}_{K_{bp}^T} \quad (11)$$

where K_b and K_p measure the correlation of the background noise and the particle pattern, and K_{bp} measures the correlation between the two components. Introducing the diagonalization $K = \Psi \Sigma^2 \Psi^T$, the singular values of the video sequence reads:

$$\Sigma^2 = \underbrace{\Psi^T K_p \Psi}_{D_p} + \underbrace{\Psi^T K_b \Psi}_{D_b} + \underbrace{\Psi^T K_{bp} \Psi}_{D_{bp}} + \underbrace{\Psi^T K_{bp}^T \Psi}_{D_{bp}^T} \quad (12)$$

To verify the validity of Assumption 2, the diagonal entries of these four terms must be analyzed. Introducing the singular value decompositions of X_b and X_p , the mixed term K_{bp} can be rewritten as

$$K_{bp} = X_b^T X_p = \Psi_b \underbrace{\Sigma_b \Phi_b^T \Phi_p \Sigma_p}_{\mathcal{W}_{bp}} \Psi_p^T, \quad (13)$$

where the elements of the weighted projection \mathcal{W}_{bp} are given by:

$$\mathcal{W}_{bp}^{ij} = \sigma_{bi} \langle \phi_{bi}, \phi_{pj} \rangle \sigma_{bj} \quad (14)$$

and have no entries for the rows $i > r$, as $\sigma_{bi} \approx 0$ (cf. Eq. (7)). Inserting Eq. (13) into Eq. (12) results in:

$$D_{bp} = \underbrace{\Psi^T \Psi_b}_{\mathcal{T}_b} \underbrace{W_{bp}}_{\mathcal{T}_p^T} \underbrace{\Psi_p^T \Psi}_{\mathcal{T}_p^T} \quad (15)$$

where $\mathcal{T}_b = \Psi^T \Psi_b$ and $\mathcal{T}_p = \Psi^T \Psi_p$ are the change of basis matrices linking the temporal evolutions of the video sequence to those of the background and particle pattern. Since the background sequence X_b has only r non-zero singular values, it is possible to neglect any temporal correlation $\mathcal{T}_b = \langle \psi_i, \psi_{bj} \rangle$ for $i > r$. Both \mathcal{T}_b and D_{bp} will thus have at most r non-zero rows and neither D_{bp} nor D_{pb} will contribute to the diagonal entries in Eq. (12) for $i > r$. Equivalently, neither will influence the singular values σ_k ($k > r$) of the image recording matrix X .

Because of the limited rank, the same argument – and conclusion – holds for the background related term $D_b = \Psi^T K_b \Psi = \mathcal{T}_b \Sigma_b \mathcal{T}_b^T$. The change of basis related to the particle contribution \mathcal{T}_p , on the other hand, has a full set of rows and columns. This matrix represents the change between two orthonormal basis, and it is therefore an orthonormal matrix since $\mathcal{T}_p \mathcal{T}_p^T = (\Psi^T \Psi_p)(\Psi \Psi_p^T) = I$. Expanding the definition of D_p in Eq. (12) yields the inner product between the rows of \mathcal{T}_p , weighted with the singular values of X_p :

$$D_p^{ij} = \Psi^T K_p \Psi = \mathcal{T}_p \Sigma_p^2 \mathcal{T}_p^T = \sum_{k=1}^{n_t} \sigma_{pk}^2 \mathcal{T}_p^{i,k} \mathcal{T}_p^{j,k}. \quad (16)$$

Observing that all the singular values σ_{pk} are equal except the first one (Eq. (10)) allows further elaboration:

$$\mathcal{D}_p^{ij} = n_p \left(\mu_{sp}^2 n_t + \sigma_{sp}^2 \right) T_p^{i,1} T_p^{j,1} + n_p \sigma_{sp}^2 \sum_{k=2}^{n_t} T_p^{i,k} T_p^{j,k}. \quad (17)$$

Finally, factoring out the term $n_p \sigma_{sp}^2$ gives:

$$\mathcal{D}_p^{ij} = n_p \sigma_{sp}^2 \underbrace{\sum_{k=1}^{n_t} T_p^{i,k} T_p^{j,k}}_{\delta^{ij}} + \mu_{sp}^2 n_t n_p \underbrace{T_p^{1,i} T_p^{1,j}}_{\varepsilon}. \quad (18)$$

The Kronecker-delta takes into account the orthonormality of the rows of T_p . For $i = j > r$, each term $\varepsilon = T_p^{1,i} T_p^{1,j} = \langle \psi_1, \psi_{pi} \rangle^2$ must be a small parameter, as the temporal evolutions of the particle intensity distributions are poorly correlated with the temporal evolution of the first mode of the image sequence. The second term in Eq. (18) is thus negligible and the diagonal entries in \mathcal{D}_p approximate the singular values of X_p (Eq. (10)). As this is the only term in Eq. (12) having non-zero diagonal entries for $i = j > r$, Assumption 2 is proven.

2.3. Proposed algorithm and error estimation

Since $r \ll n_t$ and $\sigma_{pk} \approx \sigma_{pk+1}$ (Assumption 1), it is possible to approximate the ideal PIV video sequence X_p underlying the video sequence X (Eq. (6)) filtering out its first r POD modes:

$$X_p = \sum_{k=1}^{n_t} \phi_{pk} \sigma_{pk} \psi_{pk}^T \approx \tilde{X}_p = \sum_{k=r+1}^{n_t} \phi_{pk} \sigma_{pk} \psi_{pk}^T. \quad (19)$$

Moreover, since $\sigma_k \approx \sigma_{pk} \forall k \in [r, n_t]$ (Assumption 2), it is reasonable to expect the decomposition of X to be aligned with that of X_p for $k > r$. Therefore, using Eq. (5) yields:

$$\tilde{X}_p \approx \tilde{X} = \sum_{k=r+1}^{n_t} \phi_k \sigma_k \psi_k^T = \tilde{\Phi} \tilde{\Phi}^T X, \quad (20)$$

where $\tilde{\Phi} = [\phi_{r+1}, \dots, \phi_{n_t}]$ is the basis for the reduced order model of X . In addition to the equality of singular values, the modes approximating the PIV pattern should have a temporal dependence ψ_k , orthonormal to $\psi_{p1} = \mathbf{1}$, i.e. $\langle \psi_k, \mathbf{1} \rangle = \sum_{j=1}^{n_t} \psi_k^j = 0$, as discussed in Section 2.1. These two constraints are used to identify the $[r+1, n_t]$ POD modes approximating the PIV pattern, to be retained in the preprocessing. Then, the method consists in constructing the reduced basis onto which project the set of images (Eq. (5)). To minimize the number of background modes in case of significant difference in the illumination of two consecutive camera exposures, the algorithm should be applied independently on the two series of frames 'a' and 'b'. This also allows to limit memory requirements.

The pseudo-code of the proposed method is summarized in the Algorithm 1, where the tolerances in line 6 are set as $\varepsilon_1 = 0.01 \sigma_{pk} = 0.01 \sqrt{n_p} \sigma_{sp}$ and $\varepsilon_2 = 0.01$. An executable version of the preprocessing tool has been made available at <http://seisbris.ac.uk/~aexrt/PIVPODPreprocessing/>.

Algorithm 1. POD Filter for PIV Image preprocessing.

1:	<i>Reshape Images</i> $Im \in \mathbb{R}^{n_x \times n_y}$ in $s_i \in \mathbb{R}^{n_p \times 1}$
2:	<i>Assemble Matrix</i> $X \in \mathbb{R}^{n_p \times n_t}$
3:	<i>Compute</i> $K = X^T X$
4:	<i>Diagonalize</i> $K = \Psi \Sigma^2 \Psi^T$
5:	<i>Compute</i> $\Phi = X \Psi \Sigma^{-1}$
6:	<i>Find</i> $r : \sigma_{k+1} - \sigma_k < \varepsilon_1 \& \langle \mathbf{1}, \psi_{pk} \rangle < \varepsilon_2 \ \forall k > r$
7:	<i>Construct</i> $\tilde{\Phi} = [\phi_{r+1}, \dots, \phi_{n_t}]$
8:	<i>Compute</i> $\tilde{X} = \tilde{\Phi} \tilde{\Phi}^T X$ with $\tilde{X} = [\tilde{x}_1, \dots, \tilde{x}_{n_t}]$
9:	<i>Reshape</i> $\tilde{s}_i \in \mathbb{R}^{n_p \times 1}$ back to $\tilde{Im} \in \mathbb{R}^{n_x \times n_y}$

It is worth observing that the requirement $\sigma_{bk} \approx 0$ for $k > r$ can be generalized to $\sigma_{bk} \ll \sigma_{pk}$. This implies that the proposed algorithm can remove also uncorrelated noise from PIV images as long as its variance is much smaller than the one due to the particle pattern.

Finally, from Eq. (20) it is possible to evaluate the amount of particle pattern's energy retained in the reconstructed sequence \tilde{X} by using the Frobenius norms to define the recovery ratio R as:

$$R = \frac{\|\tilde{X}_p\|_F}{\|X_p\|_F} \approx \frac{\|\tilde{X}\|_F}{\|X_p\|_F} = \sqrt{\frac{\sum_{r+1}^{n_t} \sigma_{pi}^2}{\sum_1^{n_t} \sigma_{pi}^2}}, \quad (21)$$

where the Frobenius norm of a matrix X is defined as $\|X\|_F = \sqrt{\text{Tr}(X^T X)} = \sqrt{\sum_1^{n_t} \sigma_i^2}$. Introducing Eq. (10), the recovery ratio of the POD filtering reads:

$$R = \sqrt{\frac{(n_t - r) \sigma_{sp}^2}{\mu_{sp}^2 n_t + n_t \sigma_{sp}^2}}. \quad (22)$$

Eq. (22) can be used to estimate the error introduced by the approximations in Eqs. (19) and (20) and thus the impact of the algorithm on the PIV particle pattern. Observing that ideal PIV images are characterized by an exponential probability density distribution [43], it is possible to assume that $\sigma_{sp}^2 \gg \mu_{sp}^2$, and thus estimate the recovery ratio as $R \approx \sqrt{1 - r/n_t}$. Finally, it is interesting to observe that upon the assumption of statistical convergence, the recovery ratio does not depend on the image resolution n_p .

3. Validation

3.1. Statistical convergence of an Ideal PIV sequence

The validity of the theoretical groundwork on the decomposition of an ideal PIV sequence presented in Section 2.1 has been assessed on the basis of computer generated PIV images of different sizes n_p , image number n_t and image particle concentration C . Particle positions $P(i_p, j_p, k_p)$ are chosen randomly within a volume $i_p \in [1, n_x]$, $j_p \in [1, n_y]$, $k_p \in [-0.5, 0.5]$ and superimposed onto a perfectly dark background. The intensity in each pixel $Im(i, j)$ is defined as:

$$Im(i, j) = \sum_{p=1}^{N_p} I_L(k_p) I_p(i - i_p, j - j_p, d_p, p_f), \quad (23)$$

where N_p is the number of particles per image ($N_p = C n_p$) and I_L is the intensity of the laser sheet. I_p refers to the 2D Gaussian intensity distribution produced by a particle of d_p pixels diameter, located at (i_p, j_p) and integrated over the sensitive part of a pixel having fill factor p_f . The laser profile I_L is assumed to be Gaussian [44] and the particle intensity I_p is expressed in terms of error function [45] assuming aberration-free optics. The pixel fill factor is set to 0.7 and particle diameters are selected from a normal distribution with a mean of 2 pixels and standard deviation of 0.5 pixels. The camera's dynamic range is set to 0–255 (8 bits). The statistical convergence supporting the proposed method is tested for two particle densities, considered extreme cases for practical PIV experiments: $C_p = 0.0064$ and $C_p = 0.287$ particles per pixel (ppp), corresponding to source densities of $N_s = 0.02$ and $N_s = 0.9$. Representative images are shown in Fig. 1a and c. For these PIV sequences, the corresponding inner product matrix K_p is compared to the theoretical prediction in Eq. (9) in terms of Frobenius norm of the error for varying image size $n_p = n_x n_y$ and number of images n_t :

$$E_F = \frac{\|K_p - n_p (\mu_{ps}^2 \mathbf{1} + \sigma_p^2 I)\|_F}{\|K_p\|_F} \quad (24)$$

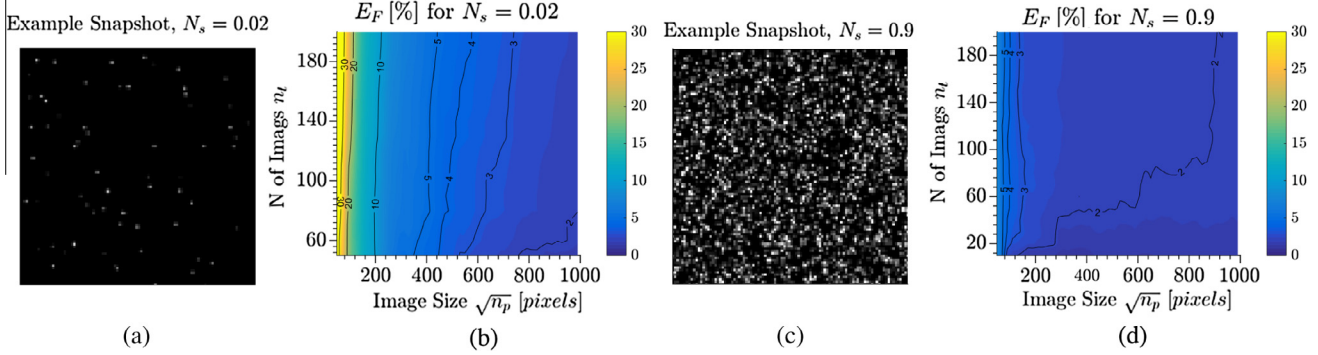


Fig. 1. Analysis of statistical convergence on synthetic PIV images with source density $N_s = 0.02$ (example in (a)) and $N_s = 0.9$ (example in (c)). (b) and (d) Compare the corresponding error maps, defined in term of Frobenius norm in Eq. (24), as a function of image size and number of images.

The Frobenius norm has been selected as performance heuristic as it gives a more severe comparison than the L_2 norm by including the entire spectrum of singular values.

Fig. 1b and d shows the resulting error maps for a set of square images. These error maps show the strong impact of particle concentration and image size on the statistical convergence whereas the number of images n_t has a weak influence. Remarkably, for a set of images of realistic size, ($\sqrt{n_p} > 600$), the theoretical inner product matrix K_p in Eq. (9) is reached within 2% of error along the entire spectrum, even at very low particle concentrations, confirming the validity of Assumption 1.

3.2. Background removal in a synthetic test case

The theoretical derivations in Section 2.2 are tested on a synthetic PIV video sequence and the background noise removal performances of the proposed image enhancement routine (Section 2.3) are compared to those of common PIV preprocessing techniques.

The sequence consists of a set of temporally unresolved $n_t = 200$ image pairs with resolution of $n_p = 1024 \times 1024$, constructed as the sum of an ideal PIV sequence X_p and a background noise sequence X_b as assumed in Eq. (6). The ideal PIV sequence X_p features the DNS simulation of a channel flow obtained from the John Hopkins Turbulence Database [46–48]. The channel flow has a Reynolds number of 4000 (based on the bulk velocity U_b and twice the half-channel height h). The entire DNS domain size is $8\pi h \times 2h \times 3\pi h$ and the velocity data is stored in a grid of $2048 \times 512 \times 1536$ points. The DNS domain is sliced in the z -direction to extract the bi-dimensional square sub-domains used in the generation of the PIV synthetic images. These sub-domains have one side corresponding to the wall and cover an area of $h \times h$ parallel to the x - y plane. The image pairs were generated with a time separation of 250 DNS time steps (corresponding to a displacement of 250 pixels on the channel centerline) and a space separation along the z -direction of 0.23 h (235 pixels). The image resolution results in 4 pixels/grid DNS points. To achieve a mean displacement on the channel centerline equal to 15 pixels, the particle displacements are multiplied by a scaling factor. The particles are spatially distributed randomly with a concentration of 0.01 ppp and diameters normally distributed with a mean of 3 pixels and standard deviation of 0.5 pixels. The laser intensity is modeled as a Gaussian with half power width equal to 4 pixels along the sheet thickness direction, in order to take into account the effect of correlation degradation due to the out-of-plane motion.

The background noise sequence X_b is obtained by random column permutation of a temporally resolved sequence X_r , constructed as the sum of four sources having a specific spatial structure $g_k(i,j)$ and temporal evolution $f_k(n)$:

$$X_r(i,j,n) = \sum_{k=1}^4 X_{rk} = \sum_{k=1}^4 f_k(n) g_k(i,j) \quad (25)$$

The first two noise sources are bounded by lines connecting the top corners with the mid-points on the opposite side ($g_{1,2}$ in Fig. 2a). Within these regions, the gray intensity levels have a Gaussian form:

$$g_{1,2} = \exp\left(\frac{-(i - i_{01,2})^2 - (j - j_{01,2})^2}{2\sigma_{g1,2}^2}\right) \quad (26)$$

centered in the top corners $(i_{01}, j_{01}) = (1, 1)$ and $(i_{02}, j_{02}) = (1, n_x)$. These Gaussians have standard deviations of respectively $\sigma_{g1} = 800$ pixels and $\sigma_{g2} = 1600$ pixels. The resulting gray level distributions are further blurred with a square Gaussian kernel of 150 pixels, leading to different levels of intensity and sharpness. These two noise sources evolve in time as squared sinusoids of the form:

$$f_{1,2}(n) = A_{1,2} \sin^2\left(\frac{2\pi}{T_{1,2}}n - \theta_{1,2} + f_{m1,2}\right) \quad (27)$$

where the periods, in terms of number of image n , are chosen as $T_1 = 15n$ and $T_2 = 33n$; the phase delays are $\theta_1 = 0, \theta_2 = \pi/2$; both amplitudes are $A_{1,2} = 100$ counts and the average intensity is $f_{m1,2} = 40$ counts. The third source g_3 simulated the omnidirectional laser light scattering caused by surface roughness, including flare, over a vertical and a horizontal line (c.f. Fig. 2a, g_3). To simulate realistic light reflection and flare, for each pixel along the defined horizontal and vertical lines, two Gaussian intensities are superimposed in the normal directions t :

$$g_3 = A_r \exp\left(\frac{-t^2}{2\sigma_r^2(i,j)}\right) + A_f \exp\left(\frac{-t^2}{2\sigma_f^2(i,j)}\right) \quad (28)$$

The reflection intensity A_r amplitude is set to equal the maximum possible grayscale (255). Prior to spatial smoothing, the widths of the intensity distributions σ_r were drawn from a normal probability with a mean of 2 pixels and standard deviation of 0.5 pixels. Flare is modeled imposing a constant standard deviation σ_f of 10 pixels with a maximum intensity A_f of 20% the maximum image intensity, followed by the spatial convolution with a Gaussian of 3 pixels in standard deviation. The resulting intensities are capped to 255 gray levels before imposing a sinusoidal temporal variation of f_3 with a period $T_3 = 5n$ and an amplitude of $A_3 = 125$ counts, producing periodical pixel saturation.

Finally, the fourth noise source $X_{b4} = g_4 f_4$ mimics the thermal camera noise, modeled as a random distribution in both time and space with a mean value of 20 counts and standard deviation of 8 counts.

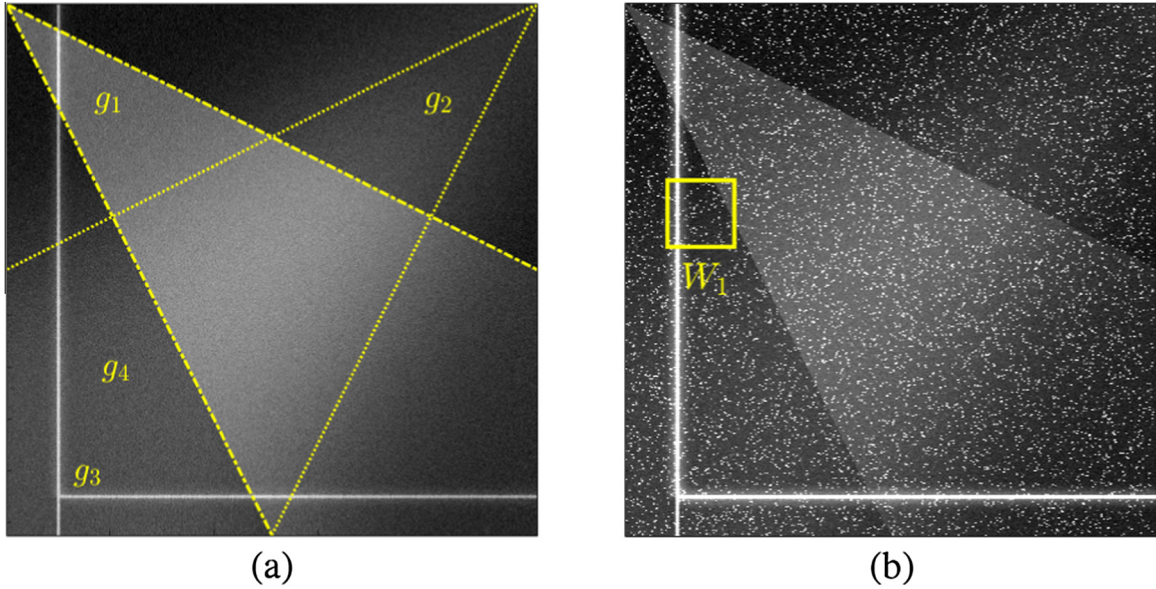


Fig. 2. Example snapshot of the background noise source X_B from Eq. (25) (a) and corresponding PIV synthetic image $X = X_B + X_p$ (b).

The singular value spectra of the video sequence $X = X_b + X_p$, the background noise sequence X_b and the ideal PIV sequence X_p are compared in Fig. 3a to the theoretical approximation in Eq. (10) for X_p .

Clearly, for $k > 5$, the singular values of the particle pattern σ_{pk} rapidly reach a constant value, in agreement with Assumption 1, while the singular values of the video sequence become $\sigma_k \approx \sigma_{pk}$, in agreement with Assumption 2. When this occurs, the singular values of the background noise rapidly drop to a constant $\sigma_{bk} \approx 31 \ll \sigma_{pk}$. Using Eq. (10b), it is easy to show that this is due to the random noise added to the background, having standard deviation of $8/256 \approx 0.031$. As this noise source also satisfies the Assumption 1, the related singular values σ_{bk} also respect Eq. (10b).

The theoretical derivations in Section 2 are therefore validated also in presence of moderate uncorrelated background noise, typical of camera sensor noise, as long $\sigma_{bk} \ll \sigma_{pk}$.

Fig. 4 compares the first temporal eigenvector of the video sequence with that of the background sequence. Indeed, regardless of the loss of temporal resolution produced by column permutation, the removed POD modes are well representative of the background noise, as expected from Eq. (20).

According to the proposed POD filtering algorithm in Section 2.3, the PIV particle pattern is well approximated by the $k \in [6, n_t]$ POD modes of the video sequence (Eq. (20)), which contains no trace of the background noise source X_b . To confirm this derivation, the background removal efficiency or the proposed method is compared to that of four popular image preprocessing techniques: the minimum intensity background subtraction [12], high pass filtering [9], contrast-limited adaptive histogram equalization (CLAHE) [19,49] and min/max recontrasting [20]. For the 128×128 window shown in Fig. 2a, the images preprocessed with each technique are juxtaposed to the original one in Fig. 5.

The minimum removal method is used separately for the two series of camera exposure a, b . The high pass filter is constructed by removing a blurred version of the images using a convolution with a squared Gaussian kernel of size 10 and standard deviation 4. The CLAHE histogram equalization is performed using the Matlab function ‘adapthisteq’ with 8×8 tiles and exponential histogram distribution with $\alpha = 5$, to reproduce the exponential distribution typical of PIV images [43]. The min/max method is applied using the Matlab function listed in [50], using a tile size of 8×8 and a level of 230 counts. The poorest removal perfor-

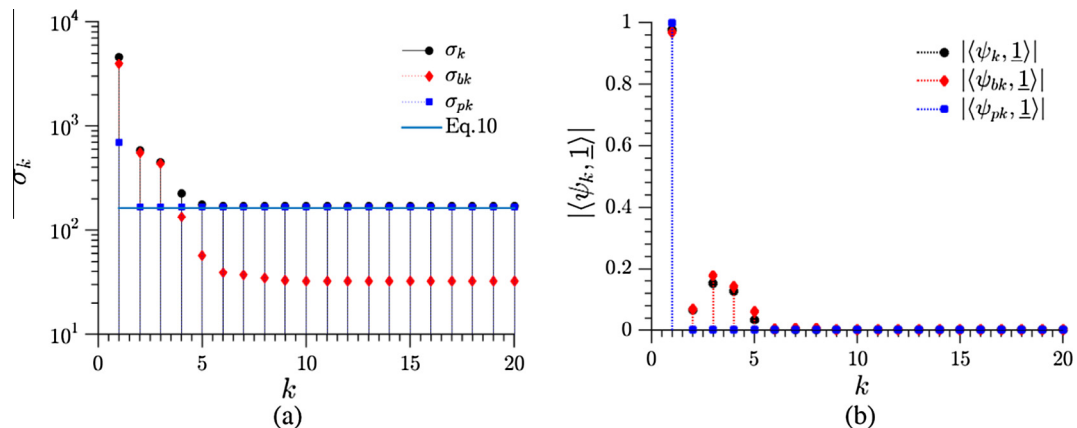


Fig. 3. Singular value spectra of the synthetic video sequence $X = X_b + X_p$, the background noise X_b , and the ideal PIV pattern X_p sequences, compared to the theoretical derivation in Eq. (10) (a). (b) Scalar products of corresponding temporal eigenvectors ψ_k, ψ_{bk} and ψ_{pk} with the first temporal eigenvector of the ideal PIV images, computed as $\psi_{p1} = 1/\sqrt{n_p} \in \mathbb{R}^{n_t \times 1}$ as derived in Section 2.1. To improve the figure readability, the plots are limited to $k \leq 20$.

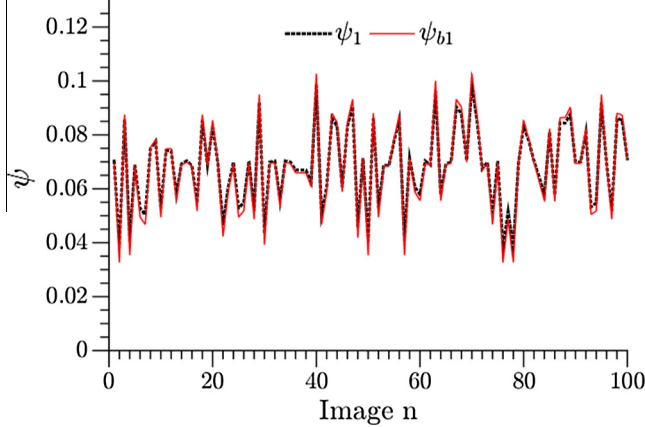


Fig. 4. Comparison of the first temporal eigenvectors for the video sequence (ψ_1) and the background noise sequence (ψ_{1b}).

mances are obtained by the minimum removal (Fig. 5b) method, due to the temporal evolution of the background noise sources considered. The high pass filtered completely removes the blurred noise source g_2 , and the random noise source pedestal g_4 , but it encounters problems on the high gradient regions of the noise

sources g_1 and g_4 . Indeed, increasing the spatial cut-off frequency improves the background removal, but at the cost of chopping the particle images in the smooth areas, and thus increasing the risk of peak locking [51]. Both CLAHE (Fig. 5d) and min/max (Fig. 5e) encounter difficulties in removing the brightest portions of the background noise, which exceeds the particle intensities. The proposed POD filter (Fig. 5f), however, is insensitive to reflection intensity, gradient and temporal variations, and the reconstructed sequence \tilde{X} approximate the particle pattern with a recovery ratio $R \approx 96\%$ (Eq. (22)). While all the background noise is completely removed, the impact on the particle image is very limited, with several particles overlying the non saturating background noise areas being entirely recovered.

The impact of the image preprocessing on the velocity fields evaluation has been analyzed using the SPIV software, developed at University of Naples Federico II [52–54]. The interrogation strategy is an iterative multi-step image deformation algorithm, with final interrogation windows of 8×8 pixels, 75% overlap. Vector validation is carried out with a universal median test [55] on a 3×3 vectors kernel and threshold equal to 2 is used to identify invalid vectors. Discarded vectors are replaced with a distance-weighted average of neighbor valid vectors. The spatial resolution achieved is realistic and consistent with that of recent PIV experiments [56], achieving a resolution of about 125×60 vectors in a $2h \times h$ domain. The averaged velocity fields obtained in the

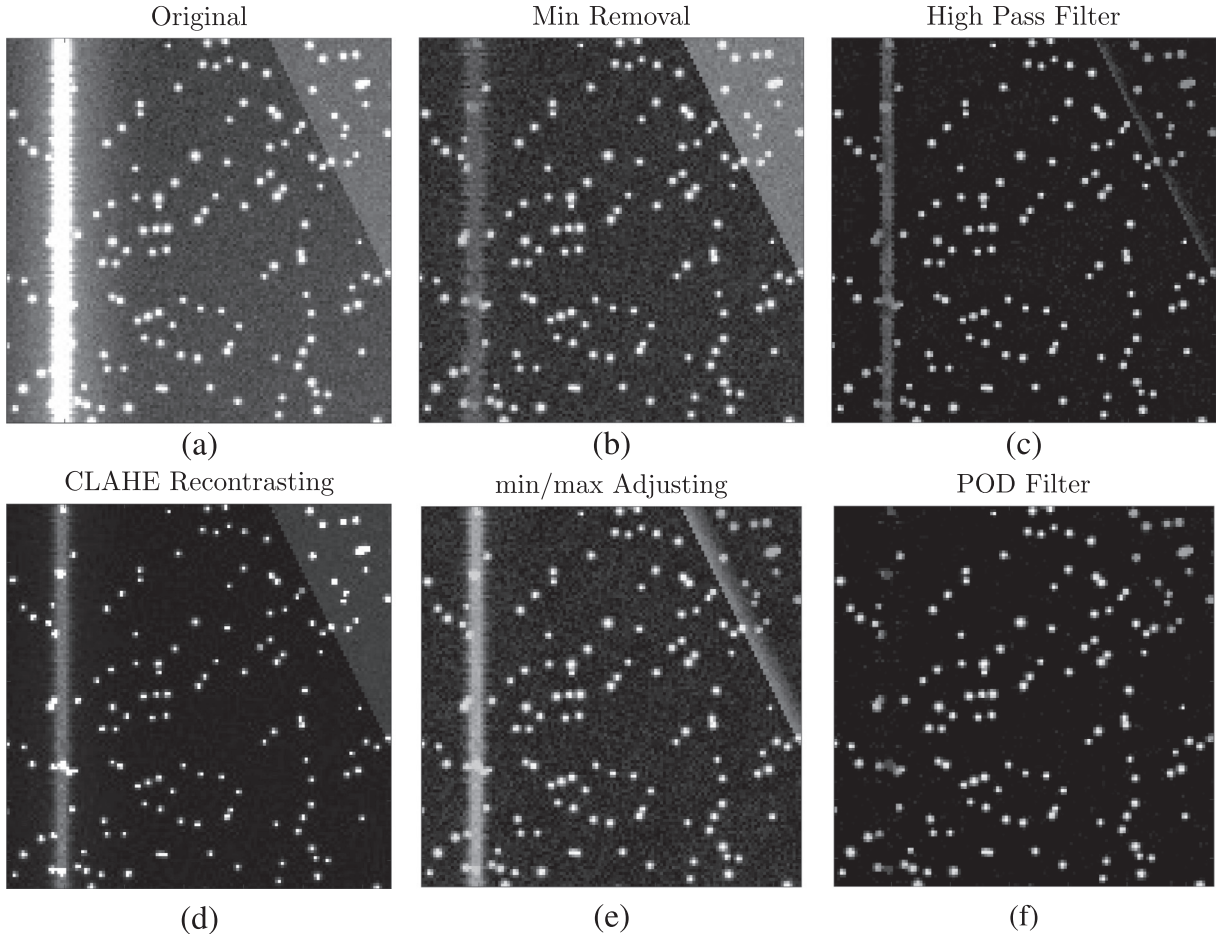


Fig. 5. Examples 256×256 image crop in the window W in Fig. 2a, showing the result of image preprocessing using historical minimum removal (a), min removal (b), high pass filtering (c), CLAHE recontrasting (d), min/max adjusting (e) and proposed POD filtering method (f). While levelization methods such as (b) and (c) performs poorly for time varying and sharp reflections, normalization methods encounter difficulties for background noise brighter than the particle images. The proposed POD filter is insensitive to both issues.

pre-processed windows in Fig. 5 are shown in Fig. 6. The contour plots compare the corresponding velocity fields with those evaluated from the ideal PIV sequence X_p , considered as reference flow field (u_{ref}, v_{ref}), in terms of velocity magnitude error:

$$Err_V = \frac{(u - u_{ref})^2 + (v - v_{ref})^2}{(u_{ref})^2 + (v_{ref})^2} \quad (29)$$

The figures title reports the number of invalid vectors (nvv) computed in the postprocessing of the window considered as those vectors for which $Err_V > 0.01$.

Indeed, the sharp and time varying edges of the noise sources g_1 and g_3 (c.f. Fig. 2a) result in a significant error in the flow field evaluation, only partially reduced by the vector validation. The flow field obtained from the original images (cf. Fig. 6a) yields up to 71% of vector for which $Err_V > 0.01$. For all the preprocessing method tested (Fig. 6b–f), the poor background removal performances are not compensated by the outliers interpolation. The best results, achieved by the CLAHE re-contrasting, features 33% of vectors with $Err_V > 0.01$. On the other hand, the flow field recovered on the images preprocessed with the proposed POD filter (Fig. 6f) matches perfectly the ideal one, with no vectors violating the Err_V validation criterion.

The computational cost of these techniques is evaluated on a PIV sequence of 1000×1000 pixels as a function of the number of images n_t in Fig. 7. All the methods are implemented on Matlab 2015 running on an Intel(TM) i7-3770 processor. While the high pass filter remains the computationally cheapest method, the cost of proposed POD filter is two orders of magnitude lower than the more advanced min/max filtering method.

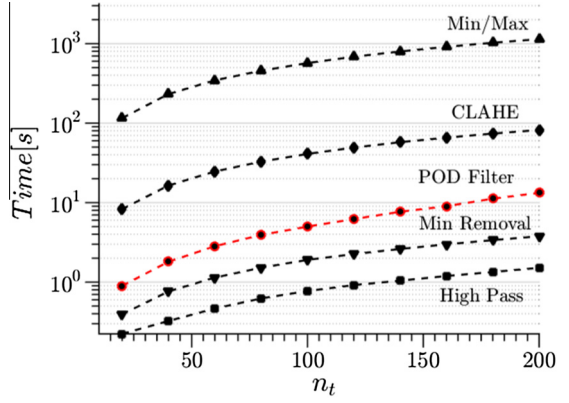


Fig. 7. Computational cost of several preprocessing methods as a function of the number of images n_t , having resolution of 1 Mpixels: min/max adjusting \blacktriangle ; CLAHE recontrasting \blacklozenge ; proposed POD filter \bullet ; ensamble minimum removal \blacktriangledown ; high pass filtering \blacksquare .

3.3. Background removal in an experimental test case

The proposed POD filtering method is tested on an experimental test case featuring moving reflections. The selected test case is the PIV investigation of the flow around a 2D flapping wing, sketched in Fig. 8.

The flapping motion of the wing consists of a translation along y , referred to as heaving, and a rotation around z , referred to as pitching. The wing profile is a NACA 0012 airfoil with a chord of

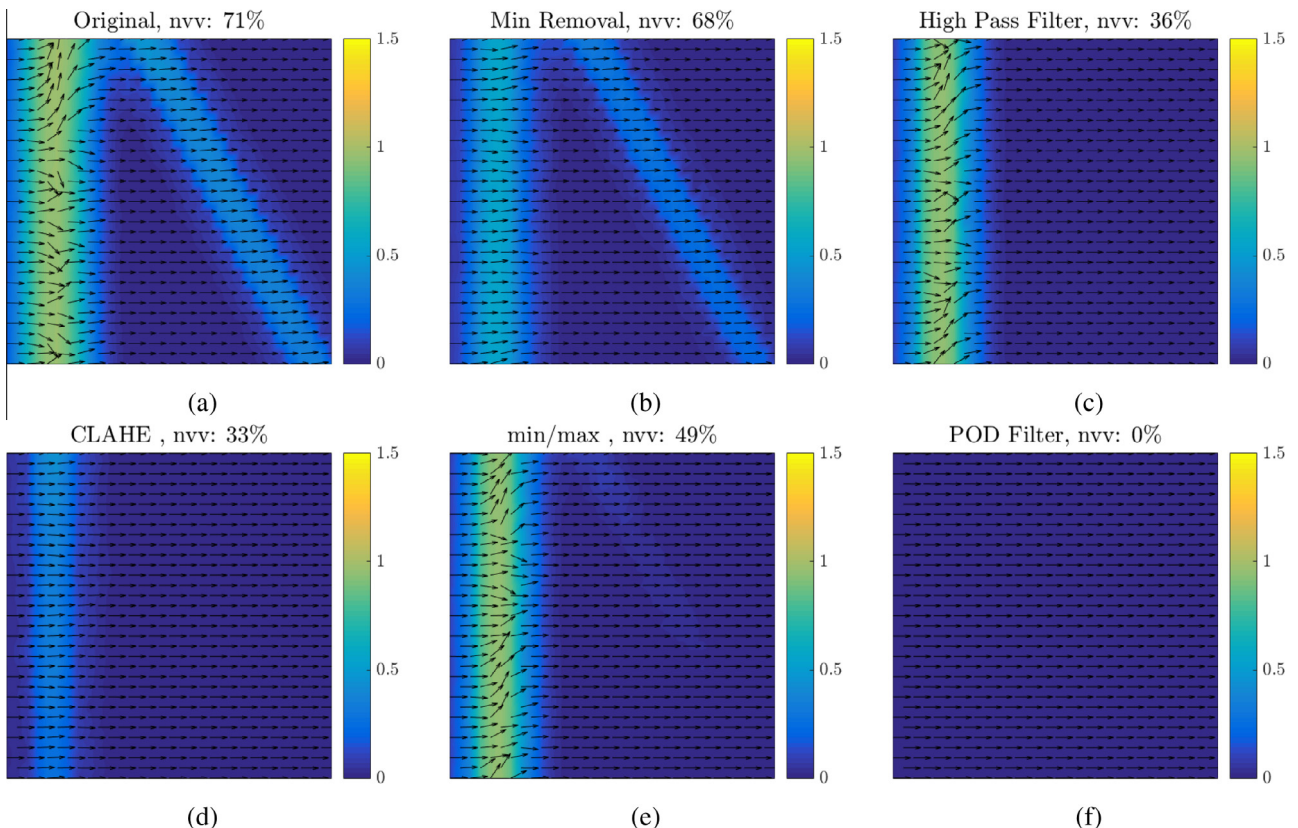


Fig. 6. Error plots in the average velocity magnitude within the 256×256 example window W in Fig. 2a for the original video sequence in (a), c.f. Fig. 5(a), historical minimum removal (b), c.f. Fig. 5(b), high pass filter (c), c.f. Fig. 5(c), CLAHE recontrasting (d), c.f. Fig. 5(d), min/max adjusting (e), c.f. Fig. 5(e), and the proposed POD filtering (f), c.f. Fig. 5(f). The velocity error is defined in Eq. (29) and the title reports the percentage of vectors, within the window, fow which $Err_V > 0.01$ (nvv).

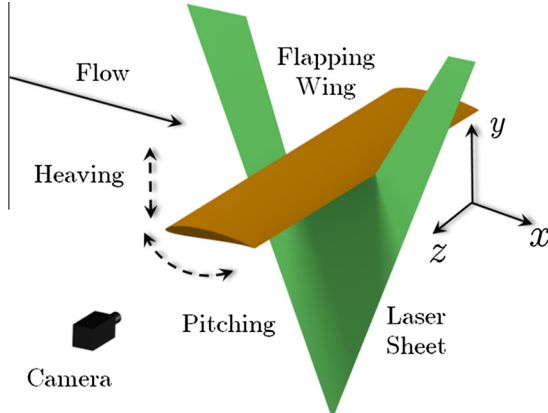


Fig. 8. Sketch of the 2D flapping wing experiment. The flow field is illuminated from the bottom, and the wing motion results in unsteady laser light reflection.

$c = 30$ mm and a span $S = 490$ mm. Heaving and pitching motions are produced by a two-rod mechanism, driven by linear actuators in periodic oscillation with an amplitude equal to the wing chord for the heaving and to 10° for the pitching.

The experiment is performed in the water tunnel at Universidad Carlos III de Madrid, which has a square cross-section of 500×500 mm². The free stream velocity is set to $U_\infty = 0.1$ m/s, corresponding to a Reynolds number $Re = U_\infty c/v = 3 \cdot 10^3$, and the flapping frequency is set to $f = 0.5$ Hz, corresponding to a Strouhal number equal to $St = cf/U_\infty = 0.3$. The flow is seeded with neutrally-buoyant polyamide particles, with 56 μm diameter. The illumination is provided by a dual cavity Nd:Yag Quantel Evergreen laser (200 mJ/pulse at 15 Hz), reshaped in a sheet with 1 mm thickness, illuminating the flow from the wing pressure side. A 5.5 Mpixels Andor sCMOS camera is used to capture $n_t = 400$ image pairs in phase-locked mode, with a resolution of about 12 pixels/mm.

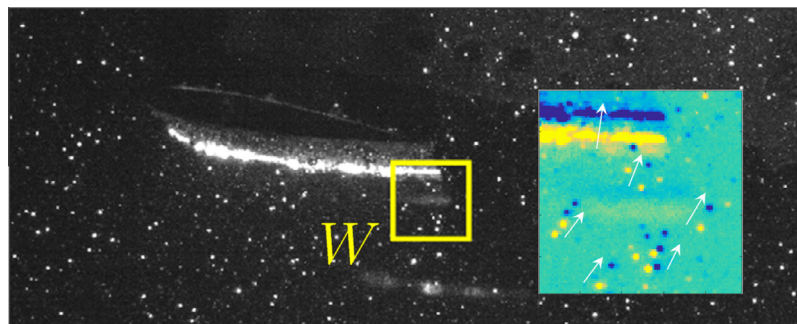


Fig. 9. Example PIV snapshot for of the PIV investigation of the flow over a flapping wing. In a 96×96 window W located close to the wing trailing edge, the image difference between two exposures is shown. Particles and wind motion are evident, with the yellow referring to the first exposure, the blue referring to the second. (For interpretation of the references to colour in this figure legend, the reader is referred to the web version of this article.)

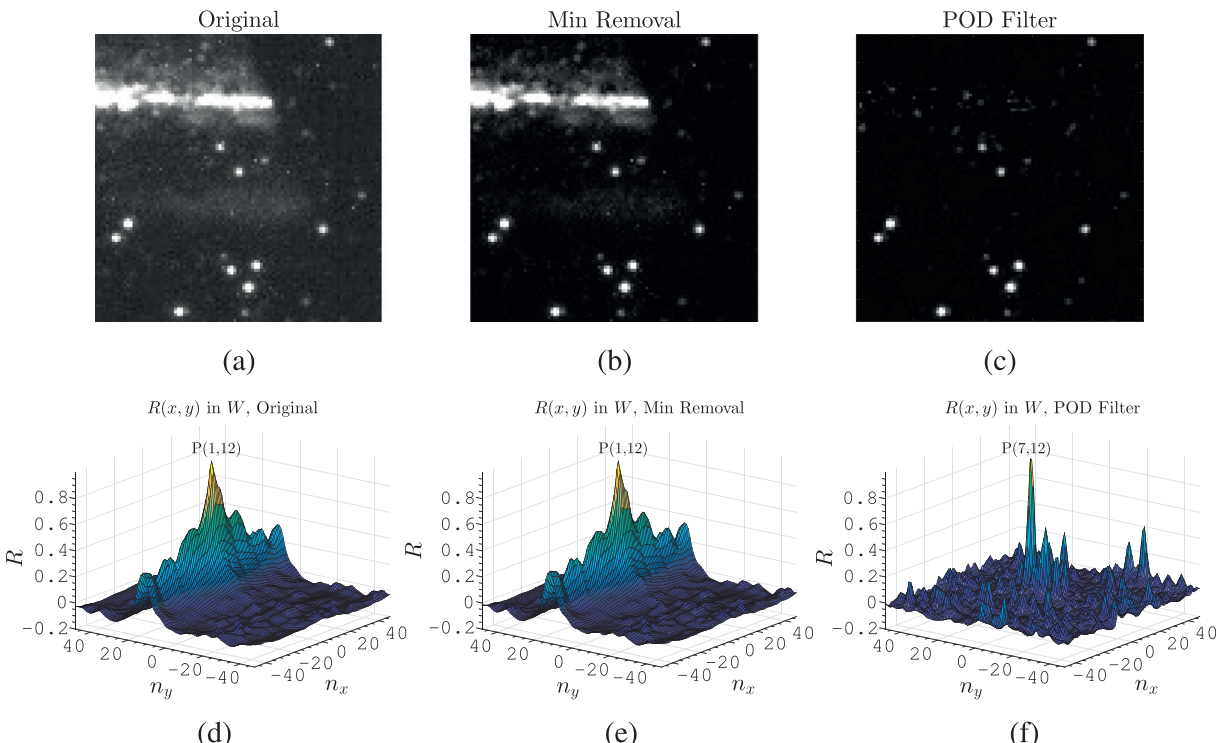


Fig. 10. Image crops from Fig. 9 for the original sequence (a) and the results of the ensemble minima removal (b) and POD filter (c). (d)–(f) Plots the corresponding cross-correlation maps. Contrary to the ensemble minima removal, the proposed POD filter is insensitive to the reflection motion produced by the wing vibration and the cross-correlation map recovers the particle displacement.

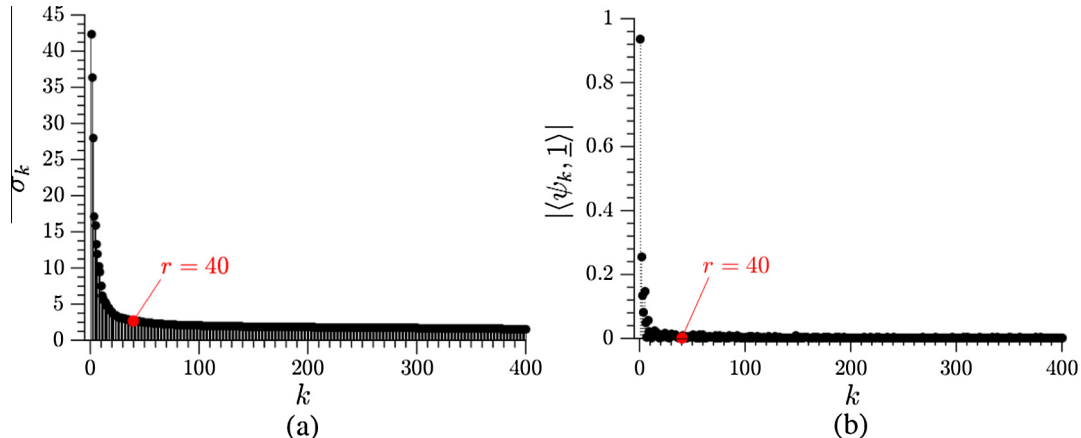


Fig. 11. Singular value spectra of the experimental video sequence for the flapping wing experiment (a); (b) scalar product of the corresponding temporal eigenvectors ψ_k with the first temporal eigenvector of the ideal PIV images, computed as $\psi_{p1} = \underline{1}/\sqrt{n_p} \in \mathbb{R}^{n_p \times 1}$ as derived in Section 2.1. For $r > 40$, the singular values become constant and the eigenvectors orthonormal to ψ_{p1} , indicating that no significant background contribution remains.

Fig. 9 shows an example PIV snapshot, including the frame difference between two consecutive exposures in a 96×96 image window located in the trailing edge area. Owing to the relatively low particle image density, particles pairs can easily be distinguished, as well as the wing displacement between two exposures. Fig. 10a shows the gray level contour in this area; Fig. 10d plots the corresponding cross-correlation map. Due to the strong intensity and the extension of the wing reflection, and the low particle concentration, the cross-correlation map is dominated by the wing motion, with a large correlation oriented along the direction of the reflection.

Despite the phase-locked acquisition, the experimental condition is rendered particularly challenging by wing vibrations, which result in unsteady laser reflections along the wing. This is evident from the weak performance of the ensemble minimum removal, which result is shown in Fig. 10b in the same image crop. As the reflection remains after the pre-processing (Fig. 10e), the cross-correlation peak due to the particles displacement remains masked by the much larger peak due to the reflection.

The pre-processing is applied to the two sequences of image exposures 'a' and 'b' independently. For the sequence of images *a*, Fig. 11a plots the singular value spectra; Fig. 11b plots the scalar product of the temporal eigenvectors with the constant vector $\underline{1}/\sqrt{n_p} \in \mathbb{R}^{n_p \times 1}$. The proposed algorithm (Section 2.3) is used with $\epsilon_1 = 0.0001\sigma_1$ and $\epsilon_2 = 0.001$, resulting in the removal of the first $r = 40$ modes in the sequence *a* and the first $r = 35$ modes in the sequence *b*. The recovery ratio (cf. Eq. (22)) is $R \approx \sqrt{1 - 40/400} \approx 95\%$.

The algorithm drastically removes the reflection without altering the particle image brightness appreciably, as shown in Fig. 10f. As no significant background contribution appears on the cross-correlation map (Fig. 10f), the particle displacement peak is recovered consistently with the particles displacements observed in Fig. 9.

4. Conclusions

A novel image preprocessing method for Particle Image Velocimetry (PIV) has been proposed. The method consists in approximating the background noise source and the PIV particle pattern with reduced order models (ROM) constructed from different portions of the video sequence's POD spectra. Particles images

and background noise are therefore distinguished according to a novel criterion: the higher degree of correlation of the background noise compared to the one of the particle pattern. The theoretical framework has been described and the fundamental assumptions supporting the method have been proven. In particular, it is shown that correlated background noise can be well approximated by a few of the first POD modes of the video, while the PIV particle pattern is equally distributed along the entire POD spectra. The proposed method is therefore a POD filter, which automatically identifies – and removes – the minimal number of modes representing the background noise. A criterion to identify the POD modes related to PIV particle patterns is given and justified theoretically. The theoretical derivations have been validated on a synthetic test case, which is also used for a comparison with existing methods in terms noise removal performances, impact on the PIV interrogation and computational cost. The results have shown that, contrary to existing techniques, the POD filter is insensitive to background noise size, intensity, gradient, and temporal oscillation. The computational cost is comparable to those of existing techniques, being one order of magnitude larger than the simple high pass filtering approach, but two orders of magnitude lower than more advanced min/max filtering. The robustness of the method has been proven on a complex experimental test case, featuring sharp, large, bright, and moving reflection over a flapping wing which strongly contributes with a sharp peak in the cross-correlation map. In this test, the proposed POD filter was capable to remove the light reflection without disturbing the particle images, and therefore allowing for recovering the particle displacements in an otherwise corrupted cross-correlation map. A downloadable version of the POD preprocessing toolbox has been made available at <http://seis.bris.ac.uk/~aexrt/PIVPODPreprocessing/>.

Acknowledgments

Miguel Alfonso Mendez is supported by a FRIA grant from the Belgian FNRS. Marco Raiola, Stefano Discetti, and Andrea Ianiro have been partially supported by Grant TRA2013-41103-P of the Spanish Ministry of Economy and Competitiveness, which includes FEDER funding. The authors wish to thank Mr. Carlos Cobos for contributing in the realization of the flapping wing experimental setup, and Eigenmann & Veronelli Iberica SL for kindly providing the polyamide particles used as PIV seeding tracers.

Appendix A. Notation and symbols

Notation	
$\langle a, b \rangle = a^T b$	Scalar product a, b
\underline{a}	Matrix with equal entries a
$\underline{\underline{a}}$	Vector with equal entries a
$A^{i,j}$	$A(i,j)$ entry of a matrix A
a^i	i -th entry of a vector a
δ^{ij}	Kronecker delta
$\ A\ _F$	Frobenious norm of matrix A
$\ A\ _2$	L_2 norm of matrix A
ρ_p	Correlation matrix
I	Identity matrix
List of symbols	
$Im(i,j)$	Grayscale image $\mathbb{R}^{n_x \times n_y}$
n_t	Number of images
d_p	Image particle diameter
p_f	Camera pixel factor
N_p	Number of particles/image
N_s	Source density
C_p	Particle concentration
n_x, n_y	Image size
$n_p = n_x n_y$	Image resolution
s_i, s_{bi}, s_{pi}	i -th columns of X, X_b, X_p
$\phi_k, \phi_{bk}, \phi_{pk}$	k -th spatial mode of X, X_b, X_p
$\psi_k, \psi_{bk}, \psi_{pk}$	k -th temporal mode of X, X_b, X_p
$\sigma_k, \sigma_{bk}, \sigma_{pk}$	k -th singular value of X, X_b, X_p
Φ, Φ_b, Φ_p	Spatial modes of X, X_b, X_p
Ψ, Ψ_b, Ψ_p	Temporal modes of X, X_b, X_p
$\Sigma, \Sigma_b, \Sigma_p$	Singular values of X, X_b, X_p
K, K_b, K_p	Inner product matrix of X, X_b, X_p
$\mathcal{T}_b, \mathcal{T}_p$	Projection of Ψ onto Ψ_b, Ψ_p
$\tilde{X}, \tilde{X}_b, \tilde{X}_p$	ROM a of matrix X, X_b, X_p
μ_{s_p}	Average in the column s_p
σ_{s_p}	Standard deviation in column s_p
R	Recovery ratio of \tilde{X} from X
I_L	Laser intensity profile
Err_V	Velocity field error
Err_r	L_2 error of $X - \tilde{X}$
I_p	Particle intensity distribution
g_k	Spatial intensity of noise source k
f_k	Temporal evolution of noise source k
T_k	Period of noise source k
σ_f, σ_r	Flare, reflection's standard deviation
A_f, A_r	Flare and reflection's amplitude
A_k	Amplitude of noise source k
(u_{ref}, v_{ref})	Velocity field from ideal PIV X_p

References

- [1] R.D. Keane, R.J. Adrian, Theory of cross-correlation analysis of PIV images, *Appl. Sci. Res.* 49 (3) (1992) 191–215.
- [2] R.D. Keane, R.J. Adrian, Optimization of particle image velocimeters: part I. Double pulsed systems, *Meas. Sci. Technol.* 1 (1990) 1202–1215.
- [3] R.D. Keane, R.J. Adrian, Optimization of particle image velocimeters: part II. Multiple pulsed systems, *Meas. Sci. Technol.* 2 (1991) 963–974.
- [4] A.M. Fincham, G.R. Spedding, Low cost, high resolution DPIV for measurement of turbulent fluid flow, *Exp. Fluids* 23 (1997) 449–462.
- [5] K. Okamoto, S. Nishio, T. Saga, T. Kobayashi, Standard images for particle-image velocimetry, *Meas. Sci. Technol.* 11 (6) (2000) 685.
- [6] A. Fincham, G. Delerce, Advanced optimization of correlation imaging velocimetry algorithms, *Exp. Fluids* 29 (1) (2000) S013–S022.
- [7] E. Paterna, P. Moonen, V. Dorer, J. Carmeliet, Mitigation of surface reflection in PIV measurement, *Meas. Sci. Technol.* 24 (5) (2013) 057003.
- [8] J.H. Lin, M. Perlin, Improved methods for thin, surface boundary layer investigations, *Exp. Fluids* 25 (5) (1998) 431–444.
- [9] C. Willert, Stereoscopic digital particle image velocimetry for application in wind tunnel flow, *Meas. Sci. Technol.* 8 (1997) 1465–1479.
- [10] M. Honkanem, H. Nobach, Background extraction from double-frame PIV images, *Exp. Fluids* 38 (2005) 348–362.
- [11] R. M-Alvarez, K.T. Christensen, Robust suppression of background reflections in PIV images, *Meas. Sci. Technol.* 24 (2013) 027003.
- [12] L. Gui, W. Merzkirch, J.Z. Shu, Evaluation of low image density recordings with the MQD method and application to the flow in a liquid bridge, *J. Flow Vis. Image Process.* 4 (1997) 333–343.
- [13] S.T. Werely, L. Gui, Advanced algorithm for microscale particle image velocimetry, *AIAA J.* 40 (2002) 1047–1055.
- [14] A. Stitou, M. Riethmüller, Extension of PIV to super resolution using PTV, *Meas. Sci. Technol.* 12 (9) (2001) 1398.
- [15] P.A. Dellenback, J. Macharivilakathu, S.R. Pierce, Contrast-enhancement techniques for particle-image velocimetry, *Appl. Optics* 39 (32) (2000) 5978–5990.
- [16] K. Zuiderveld, Contrast Limited Adaptive Histogram Equalization, in: *Graphics Gems IV*, Academic Press Professional, Inc., 1994.
- [17] D.P. Hart, Sparse array image correlation, in: *Proceedings of the 8th International Symposium on Applied Laser Technology and Fluid Mechanics*, Lisbon, 1996.
- [18] G.I. Roth, J. Katz, Five techniques for increasing the speed and accuracy of PIV interrogation, *Meas. Sci. Technol.* 12 (2001) 238–245.
- [19] U. Shavit, R.J. Lowe, J.V. Steinbuck, Intensity capping: a simple method to improve cross-correlation PIV results, *Exp. Fluids* 42 (2007) 225–440.
- [20] J. Westerweel, *Digital Particle Image Velocimetry, Theory and Practice* (Ph.D. Thesis), Delft University of Technology, 1993.
- [21] K.E. Meyer, J. Westerweel, Advection velocities of flow structures estimated from particle image velocimetry measurements in a pipe, *Exp. Fluids Suppl.* (2000) 237–247.
- [22] N.G. Deen, P. Willems, M. van Sint Annaland, J.A.M. Kuipers, R.G.H. Lammertink, A.J.B. Kemperman, M. Wessling, W.G.J. van der Meer, On image pre-processing for PIV of single- and two-phase flows over reflecting objects, *Exp. Fluids* 49 (2) (2010) 525–530.
- [23] R. Theunissen, F. Scarano, M. Riethmüller, On improvement of PIV image interrogation near stationary interfaces, *Exp. Fluids* 45 (2008) 557–572.
- [24] A. Sciacchitano, F. Scarano, Elimination of PIV light reflections via a temporal high pass filter, *Meas. Sci. Technol.* 25 (8) (2014) 084009.
- [25] C.J. Kähler, T. Astarita, P.P. Vlachos, J. Sakakibara, R. Hain, S. Discetti, R. La Foy, C. Cierpka, Main results of the 4th international PIV challenge, *Exp. Fluids* 57 (6) (2016) 1–71.
- [26] N.M. Oliver, B. Rosario, A.P. Pentland, A Bayesian computer vision system for modeling human interactions, *IEEE Trans. Pattern Anal. Mach. Intell.* 22 (8) (2000) 831–843.
- [27] T. Bouwmans, A. Sobral, S. Javed, S. Ki Jung, E.-H. Zahzah, *Handbook of Robust Low-Rank and Sparse Matrix Decomposition: Applications in Image and Video Processing*, CRC Press Taylor and Francis Group, 2016 (Ch. Robust Principal Component Analysis via Decomposition into Low-Rank and Sparse Matrices: An Overview, p. Chapter 1).
- [28] L. Laloux, P. Cizeau, M. Potters, J.-P. Bouchaud, Random matrix theory and financial correlations, *Int. J. Theoret. Appl. Finan.* 03 (03) (2000) 391–397.
- [29] H. Kargupta, S. Datta, Q. Wang, K. Sivakumar, Random-data perturbation techniques and privacy-preserving data mining, *Knowl. Inf. Syst.* 7 (4) (2005) 387–414.
- [30] V.B. Rojko, *Features Extraction Using Random Matrix Theory* (Ph.D. Thesis), University of Louisville, 2010.
- [31] M. Raiola, S. Discetti, A. Ianiro, On PIV random error minimization with optimal POD-based low-order reconstruction, *Exp. Fluids* 56 (75) (2015).
- [32] M.A. Mendez, Oscillation of a planar gas jet impinging on a deformable wall, in: T.E. Magin (Ed.), *Review of the VKI Doctoral Research 2015–2016*, von Karman Institute for Fluid Dynamics, 2016, pp. 147–158.
- [33] G. Eckart, G. Young, The approximation of one matrix by another of lower rank, *Psychometrika* 1 (1936) 211–218.
- [34] G. Berkoz, *Studies in Turbulence*, Springer New York, New York, NY, 1992 (Ch. Observations on the Proper Orthogonal Decomposition, pp. 229–247).
- [35] J. Lumley, *Stochastic Tools in Turbulence*, Academic Press, 1970.
- [36] L. Sirovich, Turbulence and the dynamics of coherent structures. I – Coherent structures, *Quart. Appl. Math.* 45 (1987) 561–571.
- [37] K. Pearson, On lines and planes of closest fit to systems of points in space, *Philos. Magaz.* 2 (11) (1901) 559–572.
- [38] H. Hotelling, Analysis of a complex of statistical variables into principal components, *J. Educ. Psychol.* 24 (6) (1933) 417–441.
- [39] I.T. Jolliffe, *Principal Component Analysis*, Springer Series in Statistic, 2002.
- [40] A.A. Miranda, Y.-A. Le Borgne, G. Bontempi, New routes from minimal approximation error to principal components, *Neural Process. Lett.* 27 (2008) 197–207.
- [41] I. Noy-Meir, Transformations in ecological ordination: I. Some advantages of non-centering, *J. Ecol.* 61 (2) (1973) 329–341.
- [42] C.M. Bishop, *Pattern Recognition and Machine Learning*, Springer, 2006.
- [43] J. Westerweel, Theoretical analysis of the measurement precision in particle image velocimetry, *Exp. Fluids* 29 (1) (2000) S003–S012.

- [44] M. Raffael, C.E. Willert, S.T. Wereley, K. Jürgen, *Particle Image Velocimetry: A Practical Guide*, Springer, 2007.
- [45] B. Lecordier, J. Westerweel, Particle image velocimetry: recent improvements, in: Proceedings of the EUROPIV 2 Workshop held in Zaragoza, Spain, March 31–April 1, 2003, Springer, Berlin Heidelberg, 2004, pp. 145–161 (Ch. The EUROPIV Synthetic Image Generator (S.I.G.)).
- [46] Y. Li, E. Perlman, M. Wan, Y. Yang, C. Meneveau, R. Burns, S. Chen, A. Szalay, G. Eyink, A public turbulence database cluster and applications to study Lagrangian evolution of velocity increments in turbulence, *J. Turbul.* 9 (2008) N31.
- [47] H. Yu, K. Kanov, E. Perlman, J. Graham, E. Frederix, R. Burns, A. Szalay, G. Eyink, C. Meneveau, Studying Lagrangian dynamics of turbulence using on-demand fluid particle tracking in a public turbulence database, *J. Turbul.* 13 (2012) N12.
- [48] J. Graham, M. Lee, N. Malaya, R.D. Moser, G. Eyink, C. Meneveau, K. Kanov, R. Burns, A. Szalay, Turbulent Channel Flow Data Set, 2013 <<http://turbulence.pha.jhu.edu/docs/>>.
- [49] W. Thielicke, E.J. Stamhuis, Towards user-friendly, affordable and accurate digital particle image velocimetry in matlab, *JORS* 2 (1) (2014) e30.
- [50] R.J. Adrian, J. Westerweel, *Particle Image Velocimetry*, Cambridge University Press, 2011.
- [51] J. Westerweel, Fundamentals of digital particle image velocimetry, *Meas. Sci. Technol.* 8 (1997) 1379–1392.
- [52] T. Astarita, G. Cardone, Analysis of interpolation schemes for image deformation methods in PIV, *Exp. Fluids* 38 (2005) 233–243.
- [53] T. Astarita, Analysis of interpolation schemes for image deformation methods in PIV: effect of noise on the accuracy and spatial resolution, *Exp. Fluids* 40 (2006) 977–987.
- [54] T. Astarita, Analysis of weighting windows for image deformation methods in PIV, *Exp. Fluids* 43 (2007) 859–871.
- [55] J. Westerweel, F. Scarano, Universal outlier detection for PIV data, *Exp. Fluids* 39 (2005) 1096–1100.
- [56] J. Hong, J. Katz, C. Meneveau, M.P. Schultz, Coherent structures and associated subgrid-scale energy transfer in a rough-wall turbulent channel flow, *J. Fluid Mech.* 712 (2012) 92–128.